# Nuclear-blast induced nanotextures in quartz and zircon within Trinitite

Aaron J. Lussier[1,*], Sergei Rouvimov[2], Peter C. Burns[1,3], and Antonio Simonetti[1]

[1]Department of Civil and Environmental Engineering and Earth Sciences, University of Notre Dame, Notre Dame, Indiana 46556, U.S.A.
[2]Department of Electrical Engineering, University of Notre Dame, Notre Dame, Indiana, 46556, U.S.A.
[3]Department of Chemistry and Biochemistry, University of Notre Dame, Notre Dame, Indiana 46556, U.S.A.

## Abstract

The intense heat and pressure resulting from the detonation of the world's first nuclear device in the New Mexico desert, July 16, 1945, severely altered the arkosic sand, producing the fused, glassy material referred to as Trinitite. The study of Trinitite is key to the development of nuclear forensic techniques that can provide crucial information about a nuclear event, such as device composition and radionuclide distribution. Moreover, nuclear blasts are often considered analogs to catastrophic natural events such as meteorite impacts, and it is well-documented that with increasing impact severity, zircon and quartz grains deform systematically. In Trinitite, a sufficient number of primary quartz and zircon grains remain identifiable. Here, a multi-technique approach (focused ion beam, scanning electron microscopy, transmission electron microscopy, and micro-Raman spectroscopy) is employed to study the micrometer-to-nanometer-scale deformation features in altered grains of zircon and quartz to constrain blast pressure and temperature conditions. Trinitite zircon grains consistently show an outer halo of fibrous baddeleyite, radiating from a relatively unaltered core; HRTEM images show complex twinning, likely originating from an intermediate, tetragonal zirconia precursor. Trinitite quartz grains show various states of melting that appear to vary predictably with depth below the surface of the desert sand. Grains occurring deeper than ~1.5 cm are crystalline, with occasional planar fractures at the optical scale. At shallower depths, a systematic increase in quartz vitrification is observed. Considered together, these data suggest maximal temperatures in excess of 1500 °C and pressures of <10 GPa, the latter being considerably less than for any natural impact event. Taken in a broader context, the implications of this work extend toward exploiting the use of advanced imaging techniques to improve our understanding of mineral processes in extreme, non-equilibrium environments at the near-atomic scale.

**Keywords:** Trinitite, zircon, martensitic twins, baddeleyite, focused-ion beam, transmission electron microscopy, micro-Raman spectroscopy

## Introduction

The world's first nuclear detonation occurred at 05:29:45 on July 16, 1945, at the White Sands Proving grounds, a remote patch of desert in New Mexico, U.S.A. The plutonium implosion nuclear device referred to simply as "*The Gadget*" produced a blast equivalent to ~21 kt of TNT, and it was of similar design to the "Fat Man" bomb dropped on the city of Nagasaki just several weeks later on 9 August. The blast resulted in intense heat and pressure that fused the mineralogically simple arkosic desert sand (Staritzky 1950) into the post-detonation material (PDM) now referred to as "*Trinitite*." This complex material shows remarkable compositional and textural inhomogeneity from the hand sample to the nanometer scale (see Bellucci et al. 2014; Eby et al. 2015). Although the first detailed petrologic description of the Trinitite material dates back to Ross (1948), it has been little studied until the past decade. Growing interest in nuclear forensics research has resulted in increased focus on PDMs, since these may elucidate significant clues as to bomb design, fuel composition, and source and processing of fissile

materials. In the aftermath of a nuclear event, this type of forensic information could be key to identifying the responsible party (or parties), and reconstructing an accurate chain of events that resulted in the incident. Trinitite is an ideal PDM on which to work, as many of these details are known (Parekh et al. 2006; Rhodes 1986). Previous investigations have shown the success of using textural (Bellucci and Simonetti 2012; Eby et al. 2015), compositional (Bellucci et al. 2014, 2013c; Donohue et al. 2015; Eby et al. 2015; Fahey et al. 2010; Koeman et al. 2013; Wallace et al. 2013), and isotopic (Bellucci et al. 2013a, 2013b; Koeman et al. 2013) information to corroborate many of the bomb details. It has also been suggested that nuclear explosions may be analogous to natural, catastrophic events, in that similar alteration features may be observed in the affected geological materials. For instance, Eby et al. (2015) notes that Trinitite shares various characteristics with fulgerites, which are produced when lightning strikes sand, and tektites, which result from meteorite impacts.

The shock alteration of zircon and quartz grains has been extensively studied in both naturally (Chen et al. 2013; Grieve et al. 1996; Gucsik et al. 2004b; Joreau et al. 1996; Nakano et al. 2008; Pidgeon et al. 2011; Schmieder et al. 2011; Trepmann

---

2008; Trepmann and Spray 2006; Wittmann et al. 2006; Zanetti et al. 2014) and experimentally (Gratz 1984; Grieve et al. 1996; Gucsik et al. 2004a; Kusaba et al. 1985; Langenhorst 1994; Langenhorst and Deutsch 1994; Leroux et al. 1999; McMillan et al. 1992; Timms et al. 2014) shocked specimens. Cordier and Gratz (1995) also examined quartz shocked by subsurface nuclear explosions at the Sedan test by TEM and found extensive evidence of deformation in the form of crystallographically oriented planar deformation features (PDFs). Such studies have repeatedly shown that deformational (planar micro-fractures, crystallographic defects, granularization, and diaplectic glasses) and phase transitional features arise systematically with increasing temperatures and shock pressures. Observing the occurrence and distribution of such features thus proves to be a highly useful petrological tool, from which information about maximum pressure and thermal shock conditions, as well as thermal post-impact histories can be derived.

Altered, primary quartz and zircon grains occur readily in Trinitite. Here we use a combination of micro-Raman spectroscopy and various forms of microscopies (optical, scanning electron, and transmission electron) to investigate the external and internal textures in Trinitite quartz and zircon grains to constrain the pressure-temperature conditions resulting from the nuclear explosion.

## METHODOLOGY

### Trinitite material

A suite of samples of Trinitite material was acquired from the Mineralogical Research Company (www.minresco.com). Upon carefully selecting samples that showed disparate textural and mineralogical properties, a series of thick sections (~100 μm) were prepared; these have been used in multiple studies at the University of Notre Dame (Bellucci and Simonetti 2012; Bellucci et al. 2014, 2013a, 2013b, 2013c; Donohue et al. 2015; Koeman et al. 2013; Wallace et al. 2013), and consistent sample nomenclature is used here.

In Trinitite, two texturally distinct zones are commonly observed. The "*glassy side*" extends to depths of ~1–2 cm from the post-detonation desert surface. Relic grains of quartz and feldspar, and less commonly zircon and apatite, are found embedded in the glassy matrix. This region also shows the highest concentrations of bomb-derived elements such as U, Pu, Pb, and Cu (Bellucci et al. 2013b; Donohue et al. 2015; Wallace et al. 2013). The "*sandy side*" occurs at depths greater than ~2 cm and consists mostly of mineral grains showing lesser degrees of alteration and coarser textures. In this region, nearly insignificant concentrations of bomb-derived α-particle-emitting nuclides are found. For this study, as with that of Donohue et al. (2015), care was taken to select sections cut with a clear vertical orientation, such that both glassy and sandy regions were readily identifiable.

### Grain selection

Both quartz and zircon grains were initially located in thin section by conventional optical microscopy and confirmed using an EDAX Orbis micro-XRF, which mapped the [2]-dimensional distribution of Si ($K\alpha$ line) and Zr ($K\alpha$ line) over the extent of several thin sections. The maximal resolution of the Orbis system is ~30 μm, allowing easy detection of quartz grains, which are typically >100 μm in width. The small diameters of zircon grains (typically <50 μm) required further confirmation using a LEO (EVO-50) scanning electron microscope, operating (mostly) in backscatter electron mode and equipped with X-ray fluorescence detection. Sections were sputtered with Ir$^+$ to improve image quality. A selection of zircon and quartz grains, occurring in both the glassy and sandy regions are imaged in Figures 1 and 7.

### Focused-ion beam and transmission electron microscopy

A single zircon grain from glassy section of TS1 (referred to as Zr09), showing very distinct halo and core textures (Fig. 1g) was chosen for further study by FIB and TEM. A FEI Helios 600 Dual-beam Focused Ion Beam (FIB) was used

to extract the TEM foil. The location of the foil (dotted blue line, Fig. 1g) was carefully chosen, such that it would contain sufficient amounts of core and fibrous materials. The excavated trench feature sputtered during the foil extraction procedure is shown in Figure 1h. In addition, TEM foils from a representative selection of quartz grains were also prepared by FIB.

Foils were extracted, thinned, and polished to <100 nm using a Ga$^+$ beam operating between 30 and 1 keV. The prepared foil was then mounted on Cu holder and examined using a FEI Titan transmission electron microscope (TEM) operating at either 80 keV (quartz) or 300 keV (zircon). All images were processed after acquisition using the Gatan Microscopy Suite (www.gatan.com). To acquire high-resolution compositional data, the instrument was set to operate in scanning-transmission (STEM) mode and data were acquired along linear traverses using the INCA EDX system (Oxford Instruments Inc.).

### Micro-Raman spectroscopy

An NRS-5100 Jasco μ-Raman spectrometer with a 50 mW 532 nm (green) laser, equipped with a Peltier-cooled CCD detector, was used to collect spectra on selected quartz and zircon grains over the ranges of 90 to 1800 cm$^{-1}$. A 100× optical objective was used to focus the laser on the sample surface and the instrument was set to operate in quasi-backscattering mode with ~2 mW of laser power interacting with the sample surface. Repeated analysis on the same location showed no degradation of spectral quality, suggesting no sample damage occurred due to laser adsorption. The system focal length is 300 mm. The system aperture was set to 20 μm (for both spot analysis and two-dimensional mapping) and the final spectral resolution was 7.02 cm$^{-1}$ (1.83 cm$^{-1}$/pixel). Prior to all analyses, the system was calibrated to a pure Si standard (520.9 cm$^{-1}$ band). All samples were optically polished and cleaned immediately prior to data collection. Each spectrum is the average of three scans, totaling approximately one minute of integration time. Several zircon and quartz grains were subjected to detailed Raman analysis; however only spectra from representative zircon samples are shown below, and spectra from quartz are not illustrated as no useful deviation from characteristic reference spectra are displayed (e.g., RRUFF-R040031; Downs 2006).

## RESULTS

### Trinitite zircons

A selection of 20 Trinitite zircon grains were located throughout the glassy and sandy regions and imaged (secondary electrons); a representative selection of these is shown in Figure 1. Grains are generally equant, with diameters ranging from 15 to >100 μm (average 50 μm). Zircon grains typically consist of a central, massive region with no apparent deformation or fractures. The central region is mantled by fibrous material that radiates in an outward direction for distances of ~5–15 μm. Although they occur in very close proximity, no clear physical contact between the core and fibers is observed. Some zircons are characterized by a fibrous texture material extending throughout the entire grain (Fig. 1f). The outline of some grains (Figs. 1a, 1b, and 1e) appear planar with angled edges possibly consistent with the primary crystal faces, whereas others show highly irregular (Fig. 1h) or rounded (Figs. 1d and 1f) edges. Each zircon grain was examined carefully using SEM backscattered electron (BSE) imaging for the presence of any primary compositional zoning features; none were detected. The grain imaged in Figure 1d appears to show evidence of brittle fracture behavior, whereas the grain in Figure 1c shows little evidence of fibrous alteration product; here, the close proximity of the individual grains suggests they originate from a common fractured precursor grain. Figure 1g shows an SEM-BSE image of the grain selected for further study by TEM.

### Raman spectroscopy of zircon

A total of five zircon grains were examined by micro-Raman spectroscopy. Typical Raman spectra observed for both the core

and fibrous regions are shown in Figure 2 (*Zr\** indicates the locations of characteristic zircon bands). In the spectra from the core region, three characteristic (see RRUFF dabase-R10018; Downs 2006) zircon bands at ~1009, ~437, and ~357 $cm^{-1}$ are prominently visible, whereas characteristic bands at ~975 and 198–225 $cm^{-1}$ are present with very low intensity (Fig. 2a). Each of these bands is notably absent in the spectrum from the

fibrous region (Fig. 2b). In the Raman spectra corresponding to both core and fibrous regions, bands between 400 and 600 $cm^{-1}$ are present that clearly do not correspond to zircon (Figs. 2a and 2b). Variation in the intensity of the Raman bands centered at 590 and 1006 $cm^{-1}$ across the traverse indicated in Figure 1a are illustrated in Figures 2c and 2d. The band at 590 $cm^{-1}$ is relatively strong in the fibrous material and essentially absent in
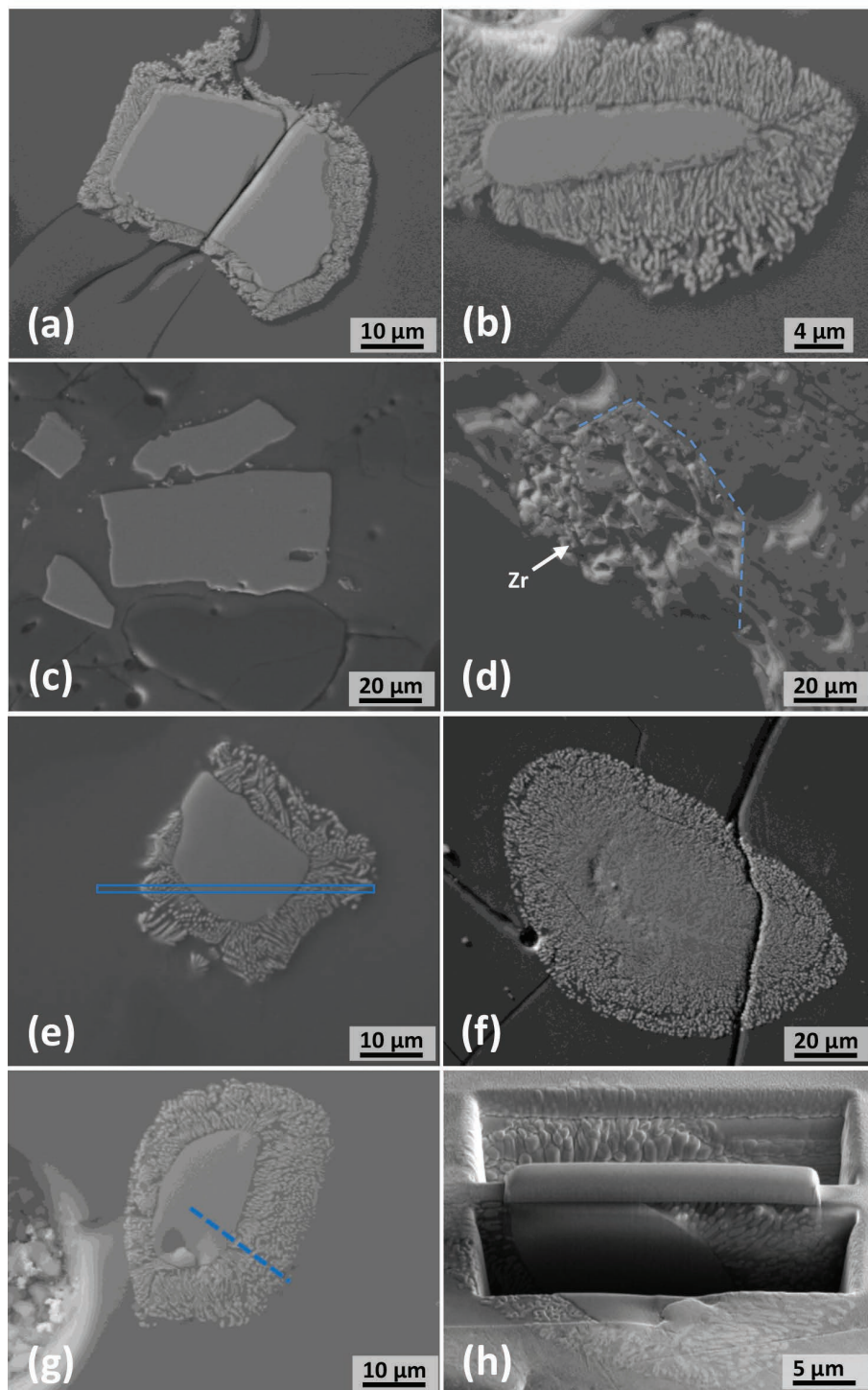


**FIGURE 1.** A selection of altered zircon grains from various Trinitite petrographic thin sections: (**a–b**) 5b 1022a (glassy section); (**c**) 5a 606b (glassy section); (**d**) 5a 606b (sandy section); (**e**) TS1 (glassy section); (**f**) 3525b (glassy section); and (**g–h**) TS1 (glassy section). The blue indicates the orientation of the TEM foil prepared by FIB.

core. Conversely, the intensity of the characteristic zircon band (at 1006 cm$^{-1}$) is consistently high in the zircon core and absent in the fibrous material.

During a natural impact event, zircons may undergo a series of phase transformations. At shock pressure exceeding 20 GPa, reidite, the high pressure ZrSiO$_4$ polymorph is typically present (Chen et al. 2013; Glass et al. 2002; Gucsik et al. 2004b; Turner et al. 2014). At temperatures exceeding 1700 °C, the decomposition of zircon to crystalline ZrO$_2$ (usually tetragonal) and amorphous SiO$_2$ occurs. Although there are at least six known ZrO$_2$ polymorphs, the ZrO$_2$ phase typically corresponds to the mineral baddeleyite (monoclinic ZrO$_2$) when observed under ambient conditions, or small volumes of the relict tetragonal phase. In natural samples, altered zircon grains may occur with a fibrous halo of baddeleyite that mantles a core of primary zircon material (Chen et al. 2003; Wittmann et al. 2006), similar to the textures observed here in Trinitite.

Comparison of the observed spectra to those of either reidite (Knittle and Williams 1993) or baddeleyite (Fig. 2f) does not yield an obvious match. For completeness, the spectra were also compared to those of other ZrO$_2$ (tetragonal, del Monte et al. 2000; isometric, RRUFF-R04142 Downs 2006; orthorhombic-I, Ravindran and Yadav 2015; cotunnite-type, Haines et al. 1997) and SiO$_2$ (tridymite, stishovite, cristobalite, coesite; RRUFF database; Downs 2006); no conclusive match was observed. As presented in greater detail below, energy-dispersive spectroscopy (Fig. 3) and high-resolution TEM (HRTEM)/selected-area electron diffraction (SAED) images collected on the fibrous material are shown in Figures 4 to 5 and (as discussed below) indicate a chemical composition and a unit cell, respectively, that are consistent only with the fibrous material being monoclinic ZrO$_2$ (baddeleyite), albeit with a cell volume reduced by ~9% from typically observed values for specimens listed in Inorganic Crystal Structure Database (2015). Reasons for the inconsistent nature of the Raman analysis cannot be resolved with the current data set; however anomalous bands resulting from photoluminescence due to the presence of trace REEs (Lenz et al. 2015), or band shifting due to phonon confinement (observed in other systems with nano-crystals; Bersani et al. 1998; Gouadec and Colomban 2007) and nano-twinning (Arora et al. 2007; Kumar et al. 2012), and the presence multiple phases are possibilities worthy of future investigation.
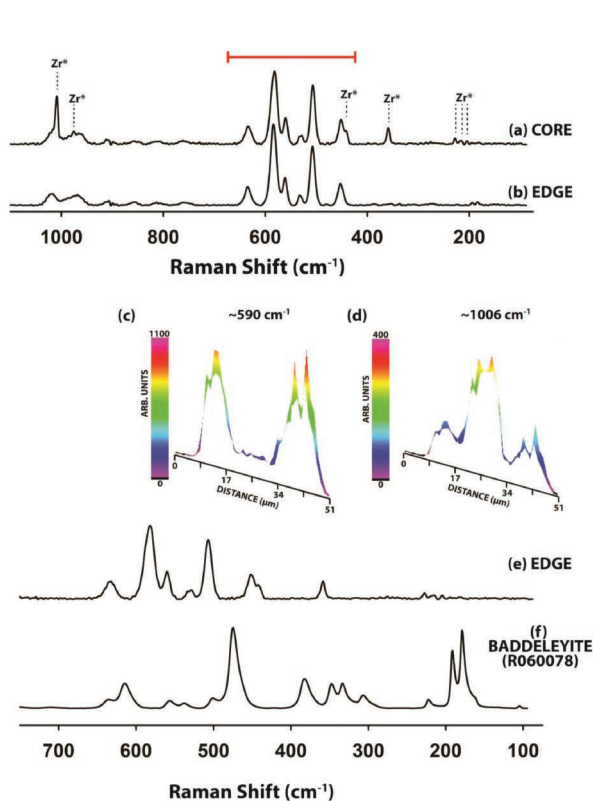


FIGURE 2. Raman spectra (532 nm) of Trinitite zircon grains. Typical spectra from zircons in Figure 1 corresponding to (**a**) core and (**b**) fibrous regions. (**c** and **d**) [2]-dimensional Raman maps plotting the intensity variation of band centered at 590 and 1006 cm$^{-1}$, respectively, for the zircon grain show in Figures 1g–1h. A comparison of band positions in the 400–650 cm$^{-1}$ of the observed, edge-region spectrum (**e**) and a baddeleyite reference taken from the online RRUFF database (specimen R060078) (**f**).
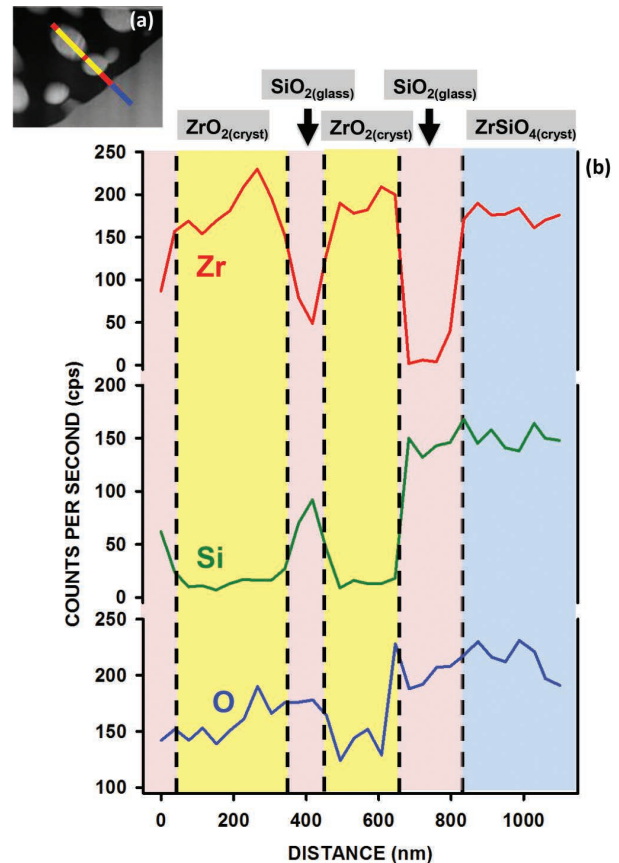


FIGURE 3. Variation in Si, Zr, and O along traverse on Zr09. The corresponding phase identities have been inset. X-ray fluorescence spectra taken with TEM operating in STEM mode. Intensity variation corresponds to band intensities for Zr (L$\alpha$, 2.04 keV), Si (K$\alpha$, 1.74 keV), and O (K$\alpha$, 0.53 keV).
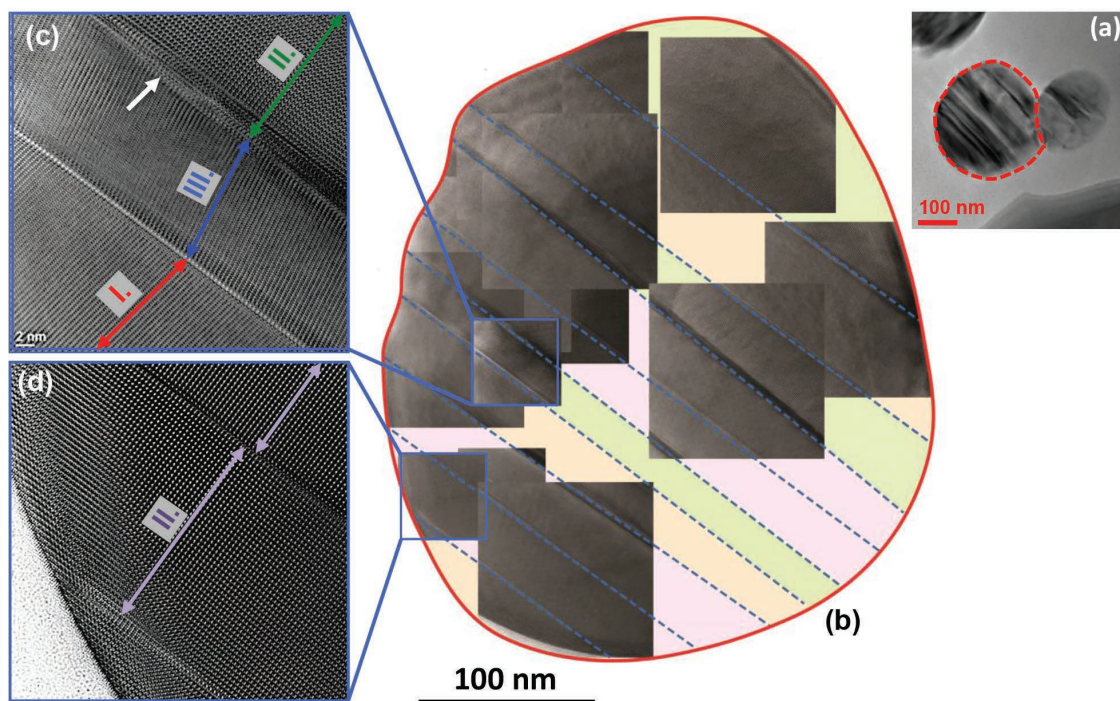
**FIGURE 4.** Detailed TEM images of a fiber cross-section. (**a**) Lower resolution image of region in Figure 6 indicated by blue arrow. (**b**) Fiber recreated by a compilation of HRTEM images. (**c–d**) HRTEM images of observed twin variants. The image clearly shows the continuity of twin planes throughout the fibers and the three structural orientations, as indicated by the orientations of the colored arrows.

### Zircon nanoscale petrography

A low-magnification TEM image of the prepared zircon foil is shown in Figure 6a, and the colored boxes correspond to regions shown at higher magnification in Figures 6b–6g. The central region appears as massive, continuous material in the lower right portion of the image. A diffraction pattern (inset lower right in Fig. 6a), corresponding to zone axis [111] confirms this phase to be zircon and an HRTEM image taken from the bulk material (Fig. 6b; red cross in Fig. 6a) shows no obvious deformation features, such as planar fractures or crystallographic defects. No diffraction was observed corresponding to the interstitial material (light gray in Figs. 6a, 6c, and 6d), confirming it to be amorphous. The variation in elemental abundances of Si, Zr, and O along the traverse section shown in Figure 3a is plotted in Figure 3b. In agreement with the phase identification by Raman spectra, the zircon core and baddeleyite fibers consists of $ZrO_2$-$SiO_2$ and of $ZrO_2$, respectively; however, the interstitial glass consists solely of $SiO_2$, and no other elements were detected.

The baddeleyite fibers occur either as elongated structures, ranging in width from 0.2 to 0.4 μm and in (apparent) length from ~0.8 to 7 μm. Several appear as circular structures, likely owing to the cross-cutting orientation of the TEM foil. The long axes of the elongated fibers are consistently oriented perpendicular to the zircon-glass interface. Images shown at higher magnifications (Figs. 6c–6g) reveal that nearly every fiber shows prominent, parallel lamellar features that crosscut the fibers at almost perpendicular angles to the long axis. These features are typically (Figs. 6d and 6g), yet not always

(Fig. 6d) continuous across the entire width of the fiber. For clarity, the TEM image shown in Figure 6a is reproduced as a trace in Figure 6h. Here, the green dotted lines indicate the average direction of the fiber axes. Two orientations of lamellae are observed, corresponding to the purple and orange lines. The sub-parallel alignment of each line color highlights the consistent orientation of lamellae across multiple, physically separated and differently oriented fibers. The majority of fibers show a lamellar orientation corresponding to the purple line, whereas only a small number show an orientation corresponding to the orange lines in Figure 6h.

Throughout the sample, the zircon/glass and baddeleyite/glass boundaries appear sharp on the sub-micrometer scale, and no well-formed crystallographic faces are observed. No fibers directly contact the central, core region; amorphous material is always present to separate the two phases. In one region, (green box in Figs. 6a and 6g) a fiber cross section appears to be pinched from the bulk core. This is the only instance in which there appears to be a clear, interaction between a fiber and the bulk zircon, although amorphous material still clearly separates the two structures. The higher-magnification image shown in Figure 6e (blue in Fig. 6a) shows the lamellar features correspond to twin planes that distinguish nanometer-scale twins of baddeleyite. The individual twins are typically between 20–30 nm in width and are in nearly perfect parallel alignment.

### Nanoscale twins in baddeleyite fibers

A partial image of a fiber cross section (blue arrow in Fig. 6a), constructed of adjacent TEM micrographs, is shown in Fig-

**FIGURE 5.** Diffraction pattern of baddeleyite twin. (**a**) the SAED pattern collected on the fiber shown in Figure 7. (**b–d**) Fourier transform calculated diffraction patterns of each twin variant; outline colors coincide with arrows in Figure 4; (**e**) summation of individual pattern shows recreates the pattern in **a**; (**f**) illustrates the indexed patterns for each of the three lattices, viewed down zone axis [010] (blue spots), [0$\bar{1}$0] (red spots), and [100] (greed spots); and (**g**) illustrates relative axial orientations of the three color-coded twin variants; the relative orientations are consistent in **e** through **g**. The (*) adjacent to reflections spots indicates those that are present but should be systematically absent.
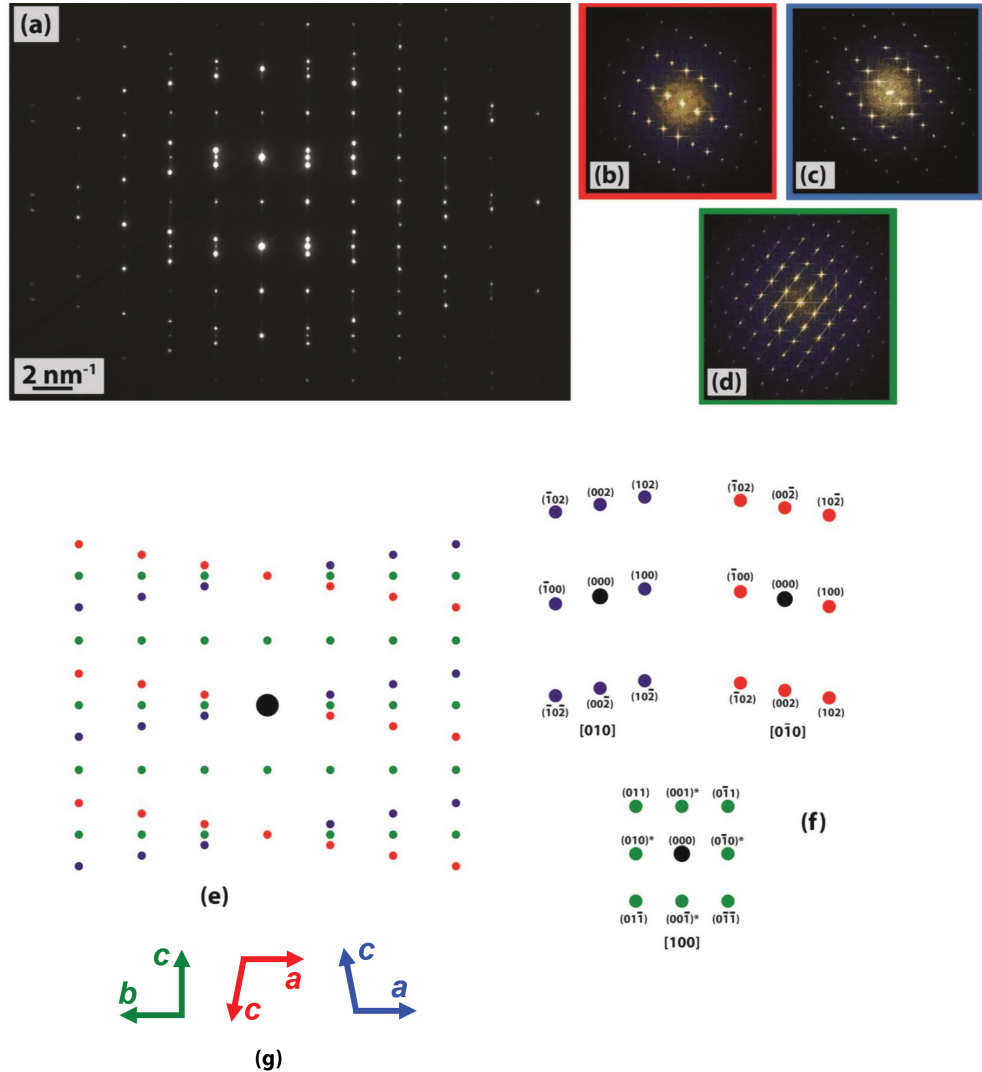


ure 4. The grain shows parallel twin planes that are continuous across the diameter; dashed blue lines highlight these planes. The HRTEM images (Figs. 4c–4d) very clearly show the twin planes and the corresponding differences in lattice orientations. The colored arrows (pink, purple, green; Figs. 4c–4d) are aligned with the lattices; they, as well as the distinctly colored backgrounds in Figure 4b, highlight the three different twin variants observed in the fiber.

Figure 5a shows a SAED image taken from the central part of the grain (i.e., a region showing all three twins). Diffraction patterns, calculated from Fourier transforms of HRTEM images of each twin variant, show the three patterns illustrated in Figures 5b–5d (note: the colors of the borders coincide with the colors of the double-headed arrows in Fig. 4). The oblique net shown in Figures 5b and 5c both correspond to the monoclinic, baddeleyite cell, imaged with electron beam down [010] (pink variant) and [0$\bar{1}$0] (green variant), respectively. The rectangular lattice (Fig. 5d) also corresponds to the baddeleyite cell, imaged with the electron beam oriented down either [100] or [$\bar{1}$00], which both correspond to indistinguishable diffraction patterns

(blue variant). Superposition of these three calculated diffraction patterns (each to correct scale) is shown schematically in Figure 5e, and the indexed patterns are presented in Figure 5f. The complex, symmetric pattern of diffraction spots observed in Figure 5a is recreated accurately only when the axial vectors of the three twin variants are aligned in the relative orientations indicated in Figure 5g.

The distribution of the three twin variants in Figures 4c–4d shows three types of adjacencies. As indicated by the double-headed colored arrows, orange-green, purple-green, and purple-purple are observed; the purple-orange adjacency is not observed (at least not in this grain). Thus, three crystallographic orientation twin relationships can be established:

(1) [100]//[100]; [010]//[0$\bar{1}$0] and (001)//(001) (red-blue),
(2) [010]//[100]; and (001)//(001) (blue-green),
(3) [100]//[$\bar{1}$00] and (001)//(00$\bar{1}$) (green-green).

The latter twin relationship occurs because the space group $P2_1/c$ lacks a mirror plane oriented along (100). The crystal

structures of baddeleyite, when projected down [100] and [$\bar{1}$00], are enantiomeric; however, the resulting electron diffraction patterns are superimposable.

The orientational relationship between the core zircon and fibrous baddeleyite material was examined by closely comparing the SAED patterns. The orientation of a zircon zone axis orientation was found using the double-tilt TEM holder. Without altering the holder orientation, diffraction patterns corresponding to multiple fibers were taken for comparison. This was done for several zircon zone axis. Crystallographic orientations of both zircon and baddeleyite were plotted in a stereonet to clearly establish orientational relationship. Shifting and rotation of the fibrous baddeleyite material, on the order or 10–15°, obscured the absolute relationship to the core zircon. However, it could be established with reasonable certainty that, with respect to the baddeleyite twin variant highlighted in red (Fig. 5), $(001)_{bd}$ was observed to contain both $[111]_{zr}$ and $[001]_{zr}$. This suggests $(001)_{bd}$ to be subparallel with $(1\bar{1}0)_{zr}$. As the (001) planes of all baddeleyite twin variants illustrated in Figures 5 and 7 exist in parallel orientation (Fig. 5g), this relation holds true for each twin. This result strongly suggests a non-random orientational relationship between the primary zircon and the fibers.
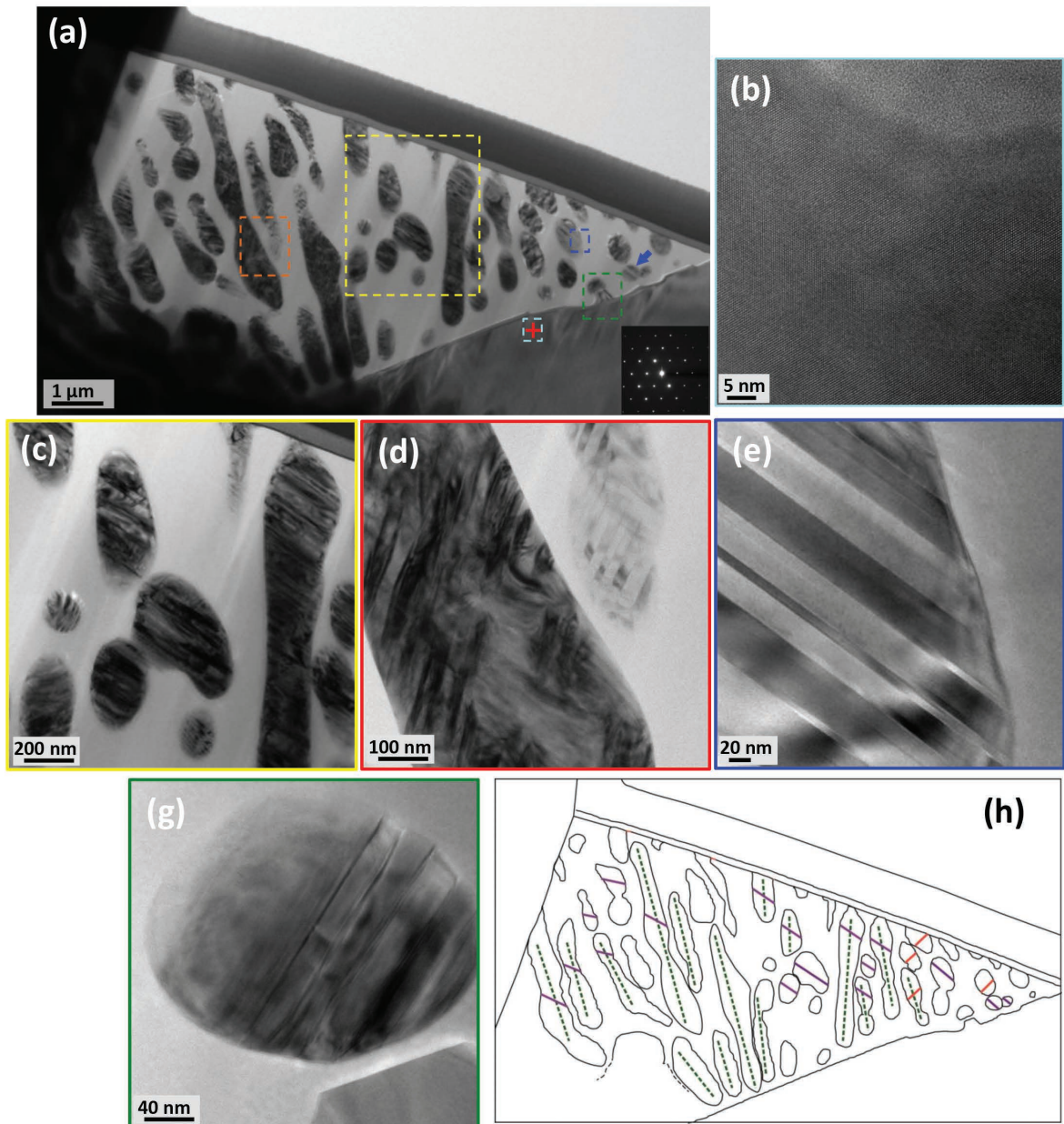


**FIGURE 6.** Transmission electron microscope of zircon foil (Zr09). (**a–g**) Images in bright-field mode; (**h**) schematic trace of **a** highlighting the orientation of fiber axes (green lines) relative to twin planes (purple and orange lines).

From the twinned diffraction image, the cell parameters for Trinitite baddeleyite can be estimated. For each parameter, 10 individual measurements were averaged, arriving at $a = 4.91(1)$, $b = 4.97(1)$, $c = 5.27(6)$, and $\beta = 99.5(5)°$, respectively. The average of 49 reported cell diameters from the ICSD is $a = 5.15(3)$, $b = 5.20(3)$, $c = 5.32(3)$ Å, and $\beta = 99.2(3)°$. Despite the relatively good agreement between these cells, the data suggest a ~9% reduction in volume compared to the average baddeleyite cell; this effect is particularly significant with respect to the $a$ and $b$ lattice parameters.

### Trinitite quartz

The regions of elevated silica (devoid of any other element) in the Trinitite thin sections indicated by XRF are initially assumed to correspond to quartz (or potentially another silica polymorph). Investigation of these regions by optical microscope, however, reveals the occurrence of three distinct types of grains.

**Type-I quartz.** These quartz grains show a characteristic, relatively sharp extinction with typical, first-order birefringence and pronounced relief, relative to the surrounding matrix of Trinitite glass. These grains range from anhedral to subhedral and from <50–200 μm in size. Physical deformation is frequently observed in type-I grains, either as cracks of irregular orientation (e.g., blue arrows, Figs. 7a–7d) or (less commonly) sets of parallel, planar deformation fractures (red arrow, Figs. 7c–7d) with a preferred orientation. Quartz grains of this type dominate the sandy areas of Trinitite sections, and are also (very rarely) observed in the glass regions.

**Type-II quartz.** These grains are predominantly anhedral and range in size from 100–200 μm. In plane-polarized light (Figs. 7e and 7h), these quartz grains show a dark, mottled core with medium relief, often surrounded by a clear, colorless rim of low optical relief. In cross-polarized light (Figs. 7f and 7h), the interiors shows discontinuous regions of mottled birefringence, however these regions show a consistent extinction angle and thus implied crystallographic continuity. Cracks of irregular orientation are often observed throughout these grains but are mostly located toward the interiors. The Becke line shows a weak difference in refractive index between this grain border and the surrounding vitrified bulk Trinitite, suggestive of partial melting. The quartz grains consistently show a highly irregular shape with edges that are significantly rounded and devoid of any obvious primary faceting. Evidence of irregular fractures are consistently observed through these grains. Grains of this type are relatively rare, corresponding to <10% of the observed quartz grains.

Detailed imaging of the type-II quartz (form Trinitite section 5a 886b) is shown in Figure 8. Here, we can see extensive vitrification in the outer region as well as the persistence of fractures of irregular orientation through the grain. Bubbles (Fig. 8b) are also present, concentrated toward the core boundary. In cross-polarized light (Fig. 8c), only the lower left region shows clear birigfringence. Detailed investigation of these grains by Raman spectroscopy shows only spectra consistent with α-quartz (spectra not shown). The clear presence of small (<10 μm) fragments of crystalline material set in a glassy matrix is observed in an SEM image of the same area (Fig. 8d).

**Type-III quartz.** The grains range in diameter from <10 to >200 μm and are highly irregular in shape, show no evidence of primary crystal faces and are mostly devoid of any fractures or other optical-scale deformation features. In plane-polarized light (Fig. 7i), this type of grain is clear and colorless. In contrast with type-II grains, the entire grain is of very low relief. In cross-polarized light (Fig. 7j), the grains appear completely isotropic with no visible extinction, indicating a lack of crystallinity. Rarely the remnants of crystalline cores are visible in the center of the grain (e.g., red arrow, Fig. 8a). The Becke line shows refractive indices to be nearly indistinguishable from that for the bulk Trinitite material. These grains are located exclusively in the glassy regions.

An example of the contact (dashed blue line) between the glassy (top) and sandy (bottom) regions is shown in Figures 7k and 7l. This image clearly shows that type-I grains are abundantly present only on the sandy side.

**Raman spectra of quartz.** In excess of a dozen quartz grains (type-I, type-II, and type–III) were studied in detail by Raman spectroscopy. Spectra were carefully examined for indications of (1) peak broadening and/or shifting resulting from exposure to shock pressure (McMillan et al. 1992), and (2) the presence of higher temperature (tridymite/cristobalite) and pressure (stishovite/coesite) polymorphs; none were observed. A series of high-resolution Raman traverses (step size <5 μm) extending from grain interiors to edges of both type-I and type-II quartz consistently yield spectra of only α-quartz. Furthermore, peak broadening/shift, relative to other published spectra of pressure-shocked quartz was not observed. Type-III grains, as well as the outer (rim) regions of type-II grains, yield Raman spectra with no discernable bands (spectra not shown).

### Quartz TEM imaging

Representative type-II and type-III quartz grains were selected for further study by TEM. The dotted red lines Figure 7 show the locations and orientations of the TEM foils extracted by FIB and imaged in Figure 9. Two examples of type-II quartz are shown, corresponding to Trinitite sections TS1 (Figs. 9a–9b) and 5a 886b (Figs. 9c–9d). The TEM images of the grain from TS1 show a highly complex deformation pattern, with non-linear veins of amorphous silica cross-cutting the grain. The crystalline area has many defects including grain boundaries and small inclusions with black-and-white contrast. There are many bending contours (dark lines) within the crystalline grains indicating the presence of residual internal strain. Micro-inclusions, as well as other deformational features are observed and may indicate phase transformation that occurs at high temperature under high-pressure conditions. The TEM image of the grain from section 5a 886b shows that the majority of the grain volume is amorphous silica (as evidenced by electron diffraction patterns). Small (0.2–1 um), highly irregular fragments of the crystalline α-quartz material occurs as islands surrounded by glass, consistent with the SEM images shown in Figure 8. In both bright-field (Fig. 9c) and dark-field (Fig. 9d) images, the remnant crystalline fragment shows bending contours (dark lines) that likely corresponding to residual internal strain, and small inclusions with black-and-white contrast due to strain around them although no obvious brittle fractures are apparent. Note that the orientation of the stress lines appears to be continuous across multiple quartz islands.
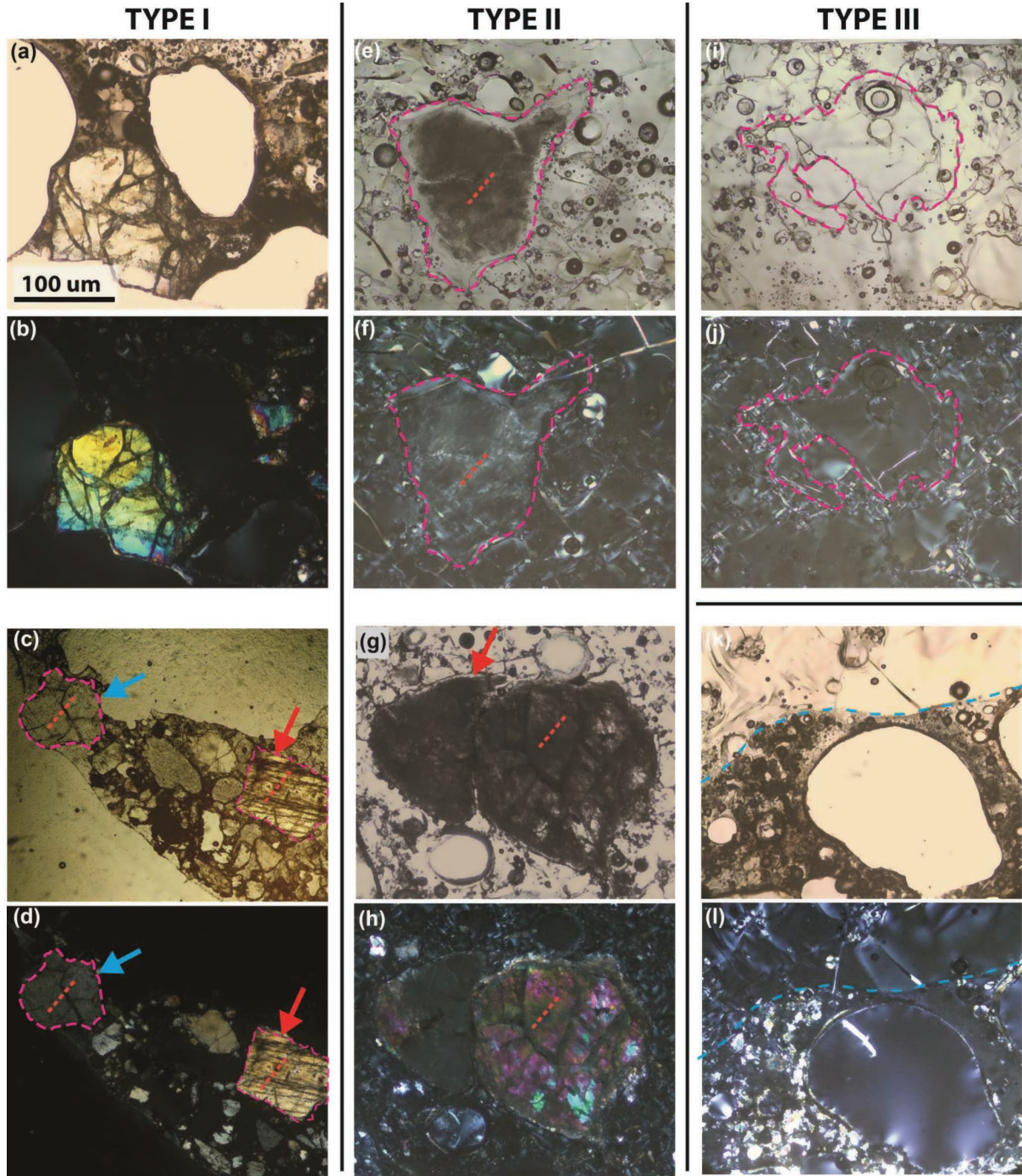
**FIGURE 7.** Optical microscope images of quartz grains taken in plane-polarized (left column) and cross-polarized (right column) light. Type-I grains from sandy regions of 5a 886b (**a** and **b**) and 5b 10.22a (**c** and **d**); type-II grains from glassy region of 5a 886b (**e** and **f**); type-III grains from glassy region of 5a 886b (**g** and **h**). The dotted pink outlines show the individual grains; the straight dotted orange lines indicate the approximate location and orientation of the TEM foil prepared by FIB. Scale of all images are as indicated in **a**.

Examples of type-I quartz grains from section 5b 10.22a are shown in Figure 9e (red arrow; Figs. 7c–7d) and Figure 9f (blue arrow; Figs. 7c–7d). In agreement with optical and Raman data, both of these grains lack any features associated with vitrification. Although both of these grains show evidence of fracture deformation under optical microscopy, features known to be related to the effects of very low-grade pressure shock (see below), the corresponding TEM images, however, show only minor physical defects. Hence, the fractures are not obviously related to the internal grain structure. This counterintuitive discrepancy has
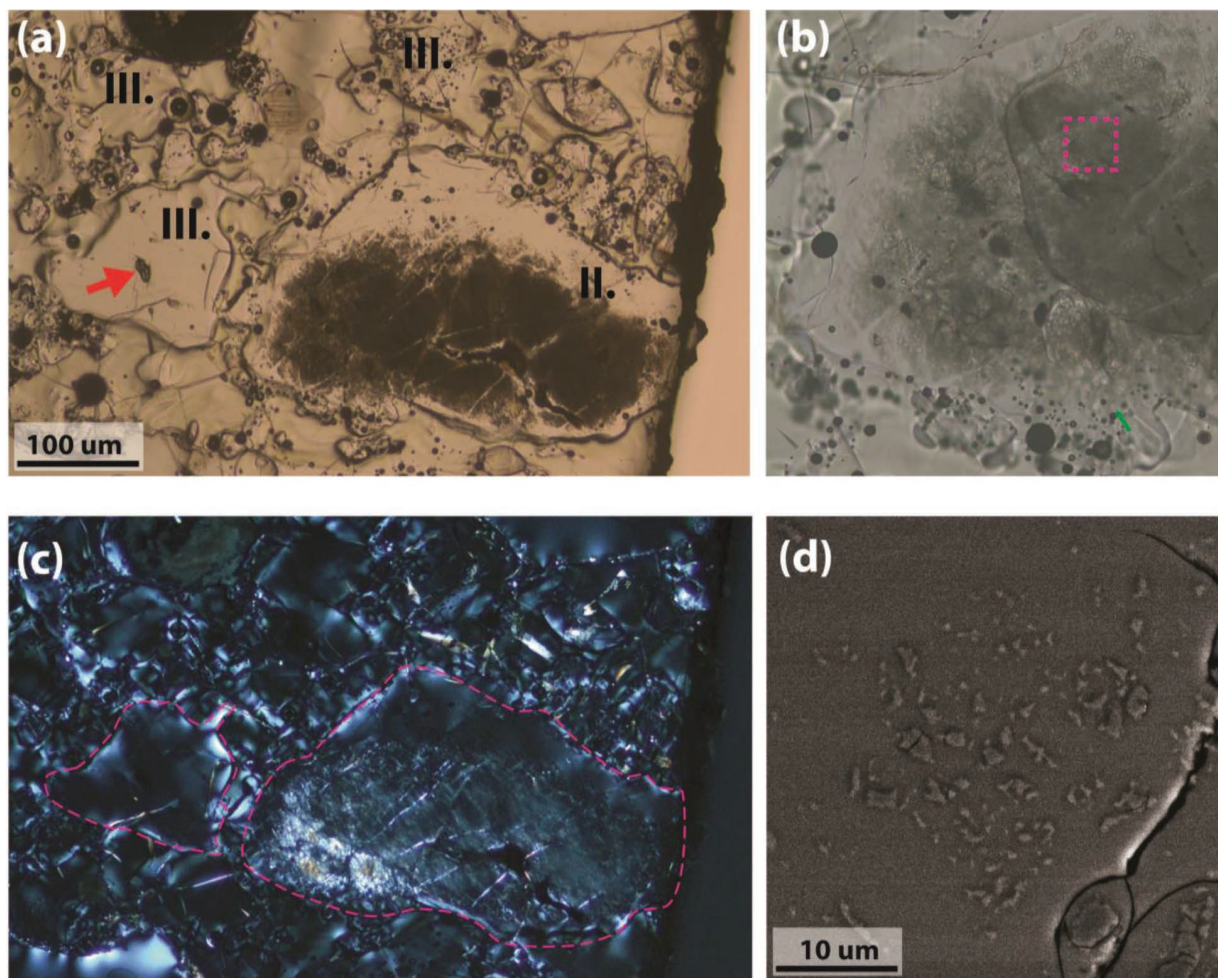
**FIGURE 8.** Images of a type-II grain from Trinitite section 5b 10.22a. (**a**) in plane-polarized light at low magnification and (**b**) at higher magnification; (**c**) in cross-polarized light showing the mottled extinction texture; (**d**) SEM image taken in backscatter mode showing the fragmentation of crystalline quartz in the glass matrix.

been noted elsewhere in the literature (Stoffler and Langenhorst 1994). These grains do, however, show shadows in bright-field images suggestive of lattice strain.

## DISCUSSION

### The origins of Trinitite constituents

Previous investigations (Bellucci et al. 2014; Donohue et al. 2015; Wallace et al. 2013) have shown that bomb-sourced radionuclides (i.e., U and Pu) are well-mixed into the vitrified material that dominates the glassy upper ~2 cm of many Trinitite samples (Fig. 10). The distribution of these elements can result from two processes: (1) the introduction of radionuclides into freshly melted desert material by the initial blast and subsequent mixing by the passing shock wave, or (2) the redeposition of melted, contaminated fallout materials. The latter process results from the ability of afterwinds (wherein cool ambient air turbulently mixes with the hot air resulting from the explosion) to carry large amounts of debris from the desert floor into the ascending fireball and mushroom cloud. The amount of debris drawn up into the mushroom cloud is approximately 0.1 Mt/

Mt (Ahearne et al. 2005) corresponding to ~2.1 Mt in the case of the Trinity device, and hence can contribute significantly to the amount of altered material observed on the desert floor. If the temperature of the hot air mass is sufficient to melt the introduced material, radioactive contaminants may become incorporated into the molten material. As the material coalesces, it is redeposited in a largely molten state in the first wave of nuclear fallout, a radioactive silicate-rich "rain." The textural and compositional complexity of Trinitite makes distinguishing between fallout and in situ processes extremely difficult, however almost certainly both did occur. This clearly complicates our ability to interpret the history of quartz and zircon grains distributed throughout the Trinitite sections. Individual mineral grains, although located very close to each other in the solidified PDM, may have experienced the blast (and immediate aftermath) in fundamentally divergent ways. Differentiating these processes is further complicated by the lack of precise data showing the distance individual specimens were sampled from the blast site. Also, it is unclear if quartz and zircon have recorded the thermal conditions experienced in the fireball/mushroom cloud, or those
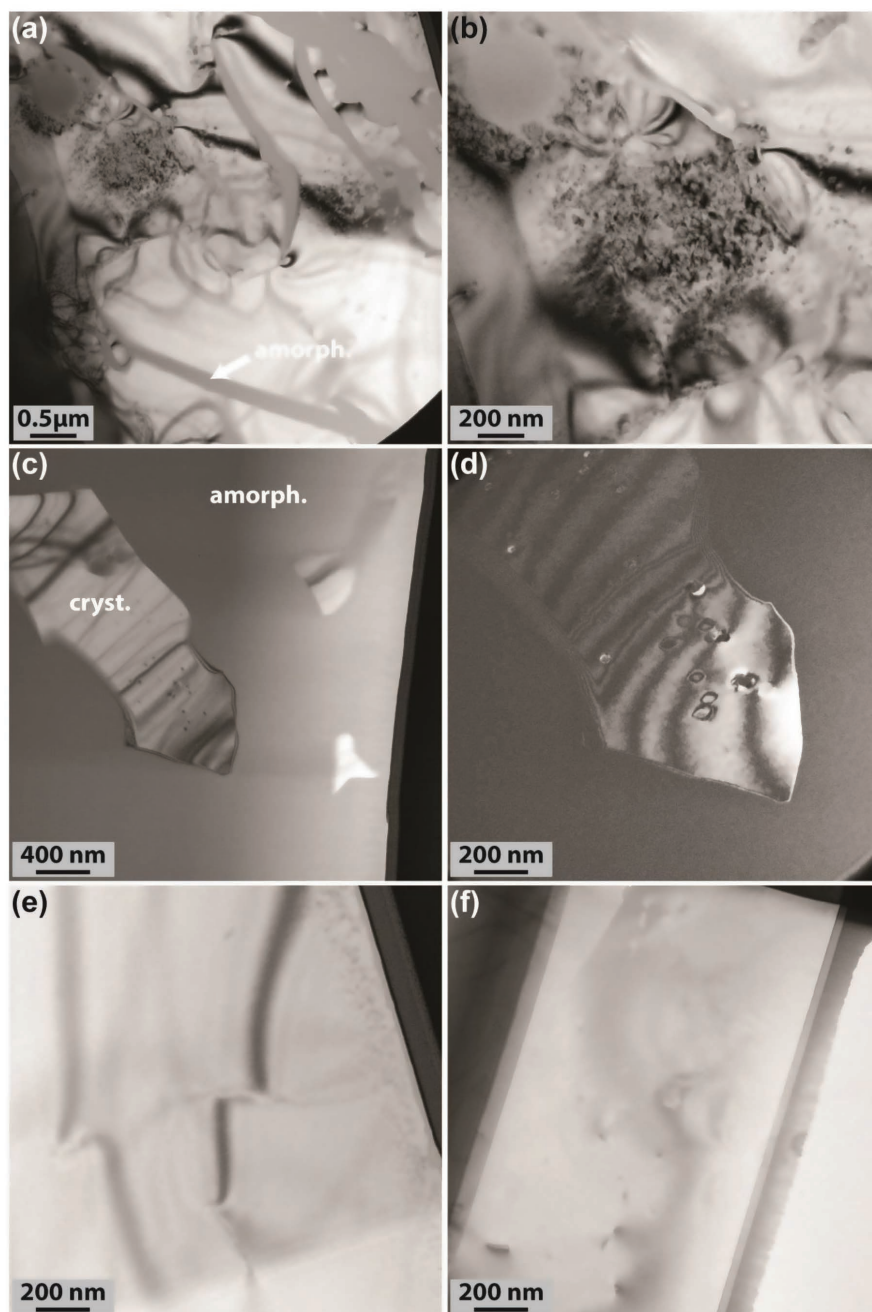
**FIGURE 9.** TEM images of quartz grains imaged in Figure 7. Images **a–b** highlight the thermal decomposition of early stage the type-II quartz grain from section TS1 imaged in Figures 7g–7h; **c–d** show bright-field and dark-field images (respectively) highlighting the advanced vitrification of quartz type-II grains from section 5b 10.22a imaged in Figures 7e–7f. Both images (**e** and **f**) show micrographs of the type-I grains in Figures 7c and 7d indicated by the red and blue arrows, respectively.

experienced by the desert floor. These issues are considered and discussed in greater detail below.

### Zircon decomposition: Temperature constraints

The SEM and TEM images reported in this study clearly show the decomposition of zircon into baddeleyite ($m$-$ZrO_2$) and silicate glass. Ambiguity persists in the literature pertaining to the temperature of thermal decomposition of zircon. Under ambient-pressure conditions, the zircon decomposition temperature has been shown to vary as a function of crystal size, purity, and heating time (Kaiser et al. 2008). Experimental studies indicate (Anseau et al. 1976; Curtis and Sowman 1953; Kaiser et al. 2008; Pavlik et al. 2001)

that, with increasing temperature, the thermal decomposition ($T_d$) of zircon occurs in two stages; decomposition begins at lower temperatures (1200–1600 °C) but with sluggish kinetics, and at $T_d$ (1550–1675 °C), the decomposition rate increases by several orders. However, even with small amounts of impurity, the value of $T_d$ may decrease significantly, largely resulting from the fact that in the $ZrO_2$-$SiO_2$ system, the eutectic and thermal decomposition temperatures differ only by ~15 °C, and impurities dramatically affect the eutectic composition.

With increasing temperatures, pure α-quartz undergoes a series of phase transformations to β-quartz (~580 °C), tridymite (~750 °C), cristobalite (~1490 °C), and melt (~1750 °C), respec-

tively. However, using this system to constrain the temperature is complicated as (1) neither Raman nor TEM data indicate the presence of higher temperature phases, despite the fact that these temperatures were clearly attained and (2) the production of diaplectic silicate glass has been observed to occur at even very low shock pressure (2.5 GPa: Kowitz et al. 2013a). Thus, the heating rate was rapid enough to result in the direct transition of α-quartz to glass at a temperature, <1750 °C, required for vitrification in thermodynamic equilibrium. After the blast, the materials apparently cooled sufficiently rapidly that no other phase could form. Also, the pressure shock wave may further affect the vitrification temperature in unpredictable ways. Furthermore, we may speculate that the delicate textures of the zircon/baddeleyite grains are more likely to have been preserved in those grains subjected to elevated temperatures while in situ.

The consistent orientational relationship between core zircon and fibrous baddeleyite material (as well as the orientational con-sistency observed with the baddeleyite fibers) material strongly suggests that the zircon material was altered to $ZrO_2$ (likely tetragonal at high temperatures—see below) without ever being detached from the primary zircon grain. This further suggests that alteration likely initiated at the grain/matrix boundary, progressing toward the grain interior.

### Shock alteration of zircon and quartz: Pressure constraints

Stoffler (1971) initially proposed that the intensity of thermal and pressure shock related to natural impact events corresponded to five (with a possible sixth) distinct stages, based largely on the Hugoniot-type behavior of framework silicates (i.e., quartz and feldspar) in non-porous crystalline rocks. In a Hugoniot-type curve, the Hugoniot Elastic Limit (HEL) corresponds to the minimum shock pressure required to induce plastic deformation. Subsequently, other work has investigated the impact-related physical deformations and phase transitions in rock-forming minerals such
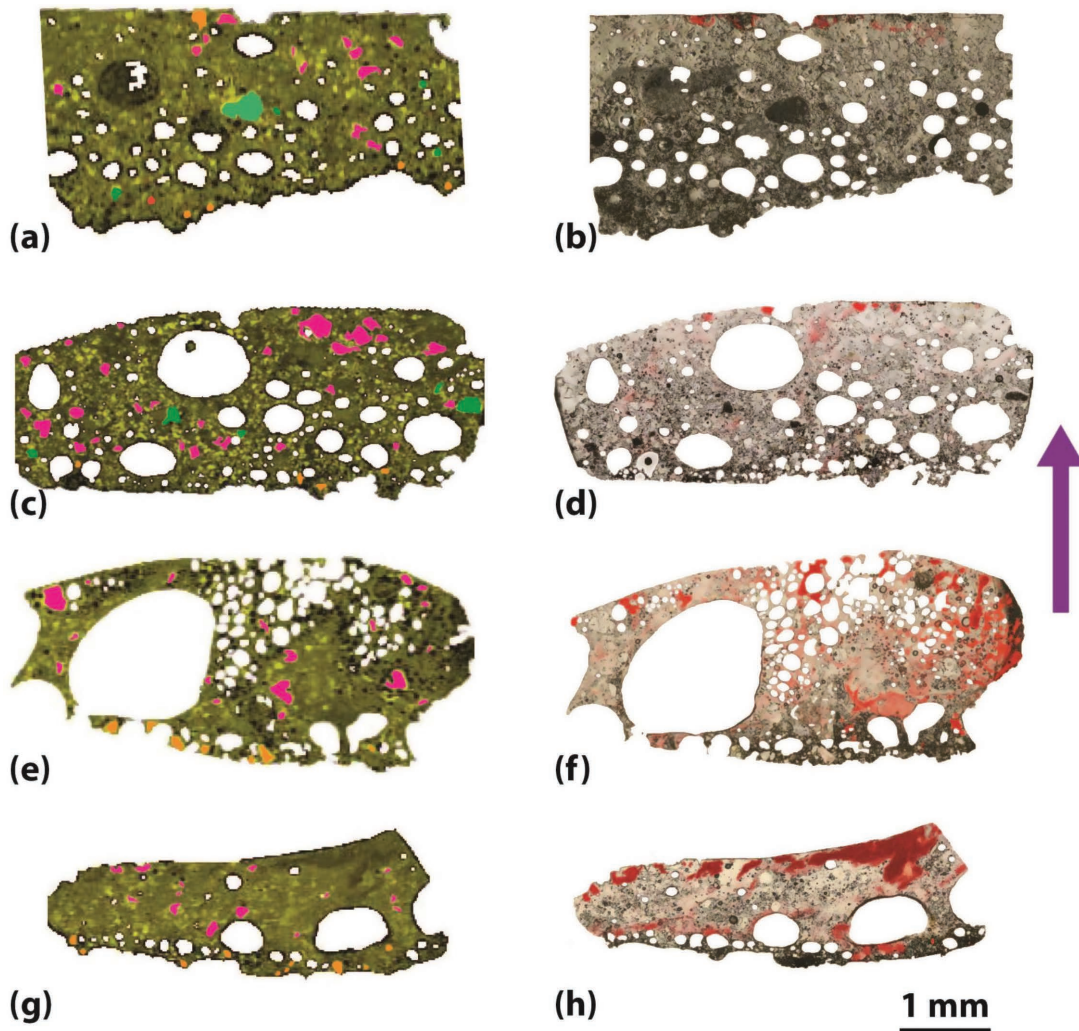


**FIGURE 10.** Alpha-track radiographs (right column) compared with distribution of quartz types (left column) in four selected Trinitite thin sections cut (approximately) vertically to the desert surface: (**a–b**) TS1; (**c–d**) 5A 8.86B; (**e–f**) 4C 8.56B; and (**g–h**) 4F 5.37A. Quartz grains are colored as follows: type-I (pink), type-II (green), and type-III (orange). The purple arrow indicates "way-up," as determined by α-track distribution.

as quartz (Cordier and Gratz 1995; Goltrant et al. 1991), zircon (Chen et al. 2013; Leroux et al. 1999; Piazolo et al. 2012; Pidgeon et al. 2011; Reimold et al. 2002; Wittmann et al. 2006; Zanetti et al. 2014), and, to a lesser extent, feldspar (Cygan et al. 1992; Huffman et al. 1993; Johnson et al. 2003; Lambert 1979; Ostertag 1983).

A predictable, systematic deformation of mineral grains is observed with increasing shock pressures and associated temperatures. A generalized, graphical representation of these shock stages as they pertain to meteorite impacts is shown in Figure 11. The black curve shows the average conditions experienced during a meteorite impact. The five shock stages, as explained above, are shown in roman numerals on the right hand side of the diagram. The encircled numbers on this figure indicate key points for both zircon and quartz deformation. At point 0, no deformational features are observed in zircon grains, but planar fractures at the millimeter scale are present in quartz grains. At point 1, planar micro-structures are observed in both quartz and zircon. Mosaicism (a highly mottled extinction texture) is commonly observed in quartz grains. Phase transitions to reidite and stishovite are also observed. At point 2, the development of diaplectic glass and coesite from quartz is prevalent, whereas in zircon, granular textures, and decorated planar microstructures are visible. At point 3, decomposition to $ZrO_2$ and amorphous $SiO_2$ occurs, and granular texture dominates the remaining zircon cores.

As mentioned above, some grains of type-I quartz show either random or planar fractures while the majority do not. Figure 11 indicates that such planar fractures to be the first deformational feature to be observed with increasing shock conditions. Other than these features, neither quartz nor zircon grains in Trinitite demonstrate evidence of physical deformational features, suggesting the HEL has not been greatly surpassed for either phase.

In porous materials, the collapsing of void spaces absorbs a significant amount of the incident shock energy. In a detailed TEM study of naturally shocked samples form the Coconino Sandstone from Meteor Crater, Arizona, moderate shocking ($10 < P < 25$ GPa) resulted in up to 50% of residual quartz grains showing fractures similar to those observed in type-I Trinitite grains, but otherwise no deformation was noted. In these natural samples, however, quartz exists in direct contact with 18–32 wt% coesite and traces of stishovite at grain boundaries. Kowitz et al. (2013) demonstrated experimentally that in natural, porous Seeberger Sandstone subjected to low-shock pressures ranging between 2.5 and 17.5 GPa, complete pore collapse and the initiation of diaplectic glass/silica melt development occurs. This is in marked contrast to the 30–35 and ~45 GPa required to induce diaplectic glass and silica melt, respectively, in single crystals of quartz (Kowitz et al. 2013b; Stoffler and Langenhorst 1994). Interestingly, Kowitz et al. (2013a, their Fig. 3) report the development of textures in quartz grains found in porous sandstones shocked to 17.5 GPa at ambient temperatures that are remarkably similar to those illustrated in Figure 8d. These authors also state that they did not observe any stishovite/coesite production and concluded this to be due to differences in experimental vs. natural pressure pulse duration and post-shock temperatures. Furthermore, systematic changes in band position (and FWHM for quartz) are observed in the Raman spectra of both zircon (Gucsik et al. 2004a) and α-quartz (McMillan et al. 1992) as pressures exceed 20 and 30 GPa, respectively. No such shifts are observed in any of the spectra collected on Trinitite specimens.

## Distribution of quartz grains types

From the above images and discussion, it seems clear that quartz grains can be placed within a continuum of increasing thermal alteration, i.e., type-I > type-II > type-III, since it is evidenced that vitrification increases, systematically from the outer edge to the inner core. The unaltered type-I quartz grains dominate the sandy regions of the Trinitite sections, and thus tend to occur in approximately their original locations in the depth profile. These grains would have experienced the shock pressure required to induce the observed, pervasive fracturing, but not the elevated temperatures required to induce melting. The partially and completely vitrified type-II and type-III quartz grains, respectively, thus correspond to material exposed to significantly higher temperatures. The persistence of type-III amorphous $SiO_2$ grains in the glassy Trinitite is somewhat contradictory. It is of interest that these grains remain discrete silicate entities, whereas the surrounding silicate material exhibits thorough melting and mixing.

One possibility is that a short time (seconds time frame) after the initial blast, the mushroom cloud temperature would decrease such that entrained desert materials remain somewhat intact with less melting. These grains were subsequently redeposited as fallout into the cooling, yet still molten, silicate matrix on the desert floor. Most redeposited quartz grains would have been completely melted (evidenced by the abundance of type-III grains), whereas some would have been only partially melted (evidenced by the rarity of type-II grains). The extent of observed vitrification in these grains is thus related to both (1) the temperature of mushroom cloud, (2) the temperature (and cooling rate) of the molten desert floor, and (3) the initial size of the grain.

This interpretation agrees with the observed distribution of quartz types in the sections shown in Figure 10. For the sections
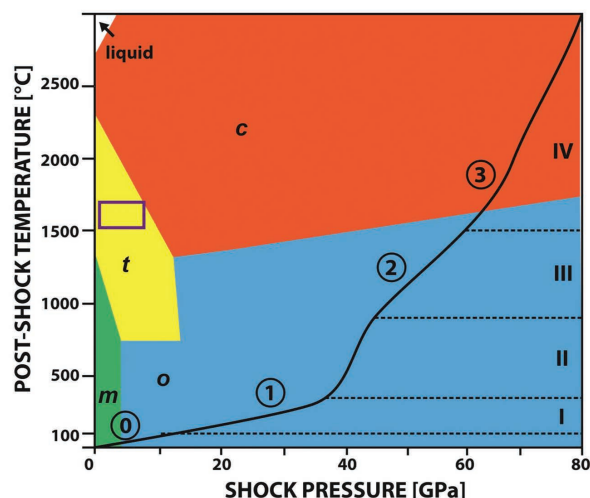


**FIGURE 11.** Pressure-temperature diagram shows the approximate distribution of significant zirconia phases as well as the typical *P-T* variation associated with impact events (modified from Wittmann et al. 2006) and the shock stages of Stoffler (1971). The dimensions of the purple box represents the maximum *P* and *T* conditions indicated by the analyses of quartz and zircon grains. Note: the superimposed zirconia phase diagram is meant mostly as a guide, as the abscissa should rightly be labeled as simply "pressure" and not shock pressure.
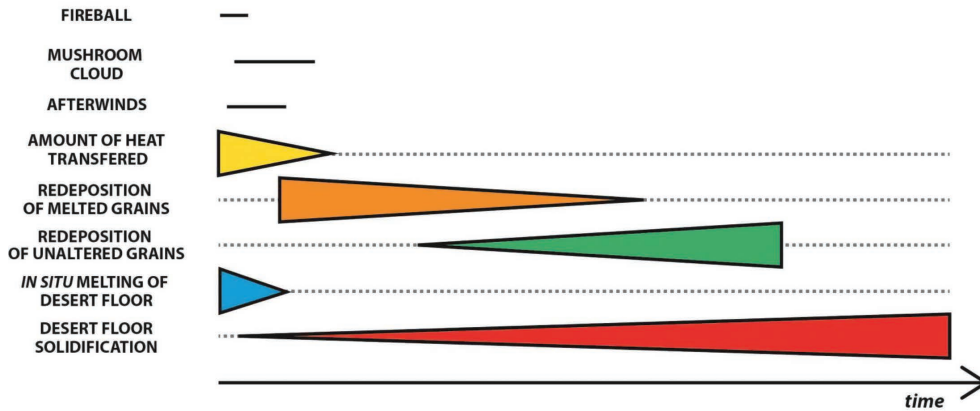
**FIGURE 12.** Schematic showing relative timing of events leading to the creation of Trinitite PDM immediately following the detonation of "The Gadget" during the Trinity test.

TS1, 4F 5.37a, 5a 8.86b, and 4C856b, the distributions of the three quartz types are shown in the images of the left column, whereas the α-track radiographs for the corresponding sections are illustrated in the images of the right column. The purple arrow indicates the vertical orientation (desert floor on top) of each of the four sections, as determined by the distribution of both α-tracks and coarser-grained/glassy material. Comparison of these images shows that the unaltered type-I quartz grains (highlighted in orange) predominantly occur in the coarse-grained "sandy" material; type-II (green) and type-III (purple) quartz grains, however, are distributed through the glassy portion. The relatively rare occurrence of type-I grains in the glassy region, likely correspond to later stage fallout, as the mushroom cloud and the desert surface cooled to temperatures insufficient to induce melting.

**Martinsitic phase transformations in the ZrO₂ system**

At the temperatures required for zircon decomposition (>1500 °C), tetragonal ZrO$_2$ ($t$-ZrO$_2$) is the stable zirconia phase (see Fig. 11). Neither TEM images nor Raman spectra show evidence for the presence of $t$-ZrO$_2$ in either the cores or the associated fibers of Trinitite zircon grains. During cooling over the temperature range of 950 to 1150 °C, a martensitic (see Lee and Rainforth 1994, and references therein) phase transformation between $t$- and $m$-zirconia is well documented. Simply stated, a martensitic phase transformation results in an overall shape change, and a habit plane, common to both parent and product phases, remains unchanged by the transition. Muddle et al. (1986) determined this plane to correspond to (130). Additionally, in the $t$-to-$m$ zirconia transition, a 5% increase in volume occurs.

The lack of any evidence indicating the presence of residual $t$-ZrO$_2$ suggests that the tetragonal phase either (1) did not crystallize at elevated temperature, or (2) has undergone a complete phase transformation to baddeleyite. Three lines of evidence support the occurrence of the latter. First, the TEM images of fibers reported here bear a high degree of visual similarity to those previously reported, examining experimentally induced $t$-to-$m$ transitions (Hannink et al. 2000; Hugo and Muddle 1993; Hugo et al. 1988; Muddle and Hannink 1986). Second, the zircon >> $t$-ZrO$_2$ >> $m$-ZrO$_2$ pathway has been demonstrated experimentally where zircon starting material has been heated to >1450 °C and cooled to ambient temperatures (Kaiser et al. 2008) with the reaction

monitored by in situ powder X-ray diffraction. The estimates of the $t$-to-$m$ transition temperatures are less than those at which the zircon decomposition occurred. Third, the development of baddeleyite twins, similar in scale to those observed here, has been proposed by Bailey (1964) to be of deformational origin, resulting from the effective stress induced by the volume increase associated with the $t$-to-$m$ martensitic transition in a constrained environment. Such stress also tends to result in the formation of microcracks, as observed along the twin planes in the HRTEM image (white arrow, Fig. 4c). The latter point suggests that as the material cooled, the Trinitite matrix was in, at least, a semi-solid state prior to the onset of the $t$-to-$m$ transition.

The orientation continuity observed between the individual baddeleyite fibers is clearly illustrated in Figure 6. This suggests that the orientations of the original $t$-ZrO$_2$ fibers were also in crystallographic continuity. Preference in crystallographic orientation often results from the application of a directional stress within the growth medium during crystallization, promoting the growth and alignment of a certain {$hkl$} form. This process is unlikely to have occurred here, as crystallographic continuity is maintained even though the orientation of different fibers changes considerably.

## IMPLICATIONS

The changes in pressure and temperature conditions associated with the detonation of a nuclear device are so rapid that establishing a sequence of events in Trinitite formation is a nontrivial endeavor. The petrographic evidence presented here allows the inference of some details of a $P$-$T$-$t$ sequence; these are shown schematically in Figure 12. During the initial blast, the temperature experienced by the desert floor rose to >1500 °C, inducing the decomposition of zircon to tetragonal zirconia and amorphous silica. The rate of cooling was sufficiently rapid to both preserve the zircon cores and prevent the transformation of α-quartz to higher temperature quenchable polymorphs.

Based on the observation made above, it appears that prior (or possibly coincident with) the onset of the $t$-to-$m$ phase transition, solidification of the bulk glassy material in the surficial "glassy" Trinitite layer began, resulting in sufficient confining pressure to induce the formation of baddeleyite micro-twins. Initial fallout was likely to have been predominantly molten, owing to the intense heat of the initial fireball and forming mushroom cloud.

As the ascending mushroom cloud cools, grains would escape with lesser degrees of melting to be deposited on the solidifying molten surface. Melting of both type-II and type-III quartz grains would continue until the temperature of the glass decreased on the desert floor sufficiently. At the later stages of fallout, no significant thermal alteration would result, and type-I quartz grains would be emplaced at very shallow depths.

Finally, both zircon and quartz are effective recorders of temperature and pressure conditions resulting from violent events such as the detonation of nuclear weapons or natural impacts. Specifically, this work shows that, when observed on the nanoscale, compositional, structural, and textural variations can greatly enhance our understanding of how such conditions evolve during, and immediately following, the event. Given their ubiquitous nature in both natural and urban environments (for quartz in particular), analogous nuclear forensic investigations conducted on future PDMs will provide important corroborating evidence in conjunction with the determination of chemical and isotopic fingerprint signatures.

## ACKNOWLEDGMENTS

## REFERENCES CITED

Ahearne, J.F., Anspaugh, L.R., Ewing, R.C., Fetter, S.A., Garwin, R.L., Gold, S.P., Grewis, E.G., Hardebeck, T.M., Jeanloz, R., Patterson, W.J., and others. (2005) Effects of Nuclear Earth-Penetrator and Other Weapons, 134 p. National Research Council, Washington, D.C.

Anseau, M.R., Biloque, J.P., and Fierens, P. (1976) Some studies on thermal solid-state stability of zircon. Journal of Materials Science, 11(3), 578–582.

Arora, A.K., Rajalakshmi, M., Ravindran, T.R., and Sivasubramanian, V. (2007) Raman spectroscopy of optical phonon confinement in nanostructured materials. Journal of Raman Spectroscopy, 38(6), 604–617.

Bailey, J.E. (1964) The monoclinic-tetragonal transformation and associated twinning in thin films of zirconia. Proceedings of the Royal Society of London Series a-Mathematical and Physical Sciences, 279(1376), 395–412.

Bellucci, J.J., and Simonetti, A. (2012) Nuclear forensics: searching for nuclear device debris in Trinitite-hosted inclusions. Journal of Radioanalytical and Nuclear Chemistry, 293(1), 313–319.

Bellucci, J.J., Simonetti, A., Wallace, C., Koeman, E.C., and Burns, P.C. (2013a) Isotopic fingerprinting of the world's first nuclear device using post-detonation materials. Analytical Chemistry, 85(8), 4195–4198.

Bellucci, J.J., Simonetti, A., Wallace, C., Koeman, E.C., and Burns, P.C. (2013b) Lead isotopic composition of Trinitite melt glass: Evidence for the presence of Canadian industrial lead in the first atomic weapon test. Analytical Chemistry, 85(15), 7588–7593.

Bellucci, J.J., Wallace, C., Koeman, E.C., Simonetti, A., Burns, P.C., Kieser, J., Port, E., and Walczak, T. (2013c) Distribution and behavior of some radionuclides associated with the Trinity nuclear test. Journal of Radioanalytical and Nuclear Chemistry, 295(3), 2049–2057.

Bellucci, J.J., Simonetti, A., Koeman, E.C., Wallace, C., and Burns, P.C. (2014) A detailed geochemical investigation of post-nuclear detonation Trinitite glass at high spatial resolution: Delineating anthropogenic vs. natural components. Chemical Geology, 365, 69–86.

Bersani, D., Lottici, P.P., and Ding, X.Z. (1998) Phonon confinement effects in the Raman scattering by $TiO_2$ nanocrystals. Applied Physics Letters, 72(1), 73–75.

Chen, J.Y., Zheng, H.F., Xiao, W.S., and Zeng, Y.S. (2003) High-temperature and high-pressure cubic zirconia anvil cell for Raman spectroscopy. Applied Spectroscopy, 57(10), 1295–1299.

Chen, M., Yin, F., Li, X., Xie, X., Xiao, W., and Tan, D. (2013) Natural occurrence of reidite in the Xiuyan crater of China. Meteoritics & Planetary Science, 48(5), 796–805.

Cordier, P., and Gratz, A.J. (1995) TEM study of shock metamorphism in quartz from the Sedan nuclear test site. Earth and Planetary Science Letters, 129, 163–170.

Curtis, C.E., and Sowman, H.G. (1953) Investigation of thermal dissociation reassociation and synthesis of zircon. Journal of the American Ceramic Society, 36(6), 190–198.

Cygan, R.T., Boslough, M.B., and Kirkpatrick, R.J. (1992) NMR-spectroscopy of experimentally shocked quartz and plagioclase feldspar powders. Proceedings of Lunar and Planetary Science, 22, 127–136.

del Monte, F., Larsen, W., and Mackenzie, J.D. (2000) Chemical interactions promoting the $ZrO_2$ tetragonal stabilization in $ZrO_2$-$SiO_2$ binary oxides. Journal of the American Ceramic Society, 83(6), 1506–1512.

Donohue, P.H., Simonetti, A., Koeman, E.C., Mana, S., and Burns, P.C. (2015) Nuclear forensic application involving high spatial resolution analysis of Trinitite cross-sections. Journal of Radioanalytical and Nuclear Chemistry, 306, 457–467.

Downs, R.T. (2006) The RRUFF Project: an integrated study of the chemistry, crystallography, Raman and infrared spectroscopy of minerals. 19th General Meeting of the International Mineralogical Association. Kobe, Japan.

Eby, G.N., Charnley, N., Pirrie, D., Hermes, R., Smoliga, J., and Rollinson, G. (2015) Trinitite redux: Mineralogy and petrology. American Mineralogist, 100, 427–441.

Fahey, A.J., Zeissler, C.J., Newbury, D.E., Davis, J., and Lindstrom, R.M. (2010) Postdetonation nuclear debris for attribution. Proceedings of the National Academy of Sciences, 107, 20207–20212.

Glass, B.P., Liu, S.B., and Leavens, P.B. (2002) Reidite: An impact-produced high-pressure polymorph of zircon found in marine sediments. American Mineralogist, 87, 562–565.

Goltrant, O., Cordier, P., and Doukhan, J.C. (1991) Planar deformation features in shocked quartz—a transmission electron-microscopy investigation. Earth and Planetary Science Letters, 106, 103–115.

Gouadec, G., and Colomban, P. (2007) Raman Spectroscopy of nanomaterials: How spectra relate to disorder, particle size and mechanical properties. Progress in Crystal Growth and Characterization of Materials, 53, 1–56.

Gratz, A. (1984) Deformation in laboratory shocked quartz. Journal of Non-Crystalline Solids, 67, 543–558.

Grieve, R.A.F., Langenhorst, F., and Stoffler, D. (1996) Shock metamorphism of quartz in nature and experiment. 2. Significance in geoscience. Meteoritics & Planetary Science, 31(1), 6–35.

Gucsik, A., Koeberl, C., Brandstatter, F., Libowitzky, E., and Reimold, W.U. (2004a) Cathodoluminescence, electron microscopy, and Raman spectroscopy of experimentally shock metamorphosed zircon crystals and naturally shocked zircon from the Ries impact crater. In H. Dypvik, M. Burchell, and P. Claeys, Eds., Cratering in Marine Environments and on Ice, p. 281–322. Springer.

Gucsik, A., Zhang, M., Koeberl, C., Salje, E.K.H., Redfern, S.A.T., and Pruneda, J.M. (2004b) Infrared and Raman spectra of $ZrSiO_4$ experimentally shocked at high pressures. Mineralogical Magazine, 68, 801–811.

Haines, J., Leger, J.M., Hull, S., Petitet, J.P., Pereira, A.S., Perottoni, C.A., and daJornada, J.A.H. (1997) Characterization of the cotunnite-type phases of zirconia and hafnia by neutron diffraction and Raman spectroscopy. Journal of the American Ceramic Society, 80, 1910–1914.

Hannink, R.H.J., Kelly, P.M., and Muddle, B.C. (2000) Transformation toughening in zirconia-containing ceramics. Journal of the American Ceramic Society, 83, 461–487.

Huffman, A.R., Brown, J.M., Carter, N.L., and Reimold, W.U. (1993) The microstructural response of quartz and feldspar under shock loading at variable temperatures. Journal of Geophysical Research: Solid Earth, 98, 22,171–22,197.

Hugo, G.R., and Muddle, B.C. (1993) Application of the crystallographic theory to the tetragonal to monoclinic transformation in ceria-zirconia. In C.M. Wayman and J. Perkins, Eds., Proceedings of the International Conference on Martensitic Transformations, p. 665–670.

Hugo, G.R., Muddle, B.C., and Hannink, R.H.J. (1988) Crystallography of the tetragonal to monoclinic transformation in ceria-zirconia. Materials Science Forum, 34-36, 165–169.

Johnson, J.R., Horz, F., and Staid, M.I. (2003) Thermal infrared spectroscopy and modeling of experimentally shocked plagioclase feldspars. American Mineralogist, 88, 1575–1582.

Joreau, P., French, B.M., and Doukhan, J.C. (1996) A TEM investigation of shock metamorphism in quartz from the sudbury impact structure (Canada). Earth and Planetary Science Letters, 138(1-4), 137–143.

Kaiser, A., Lobert, M., and Telle, R. (2008) Thermal stability of zircon (ZrSiO4). Journal of the European Ceramic Society, 28(11), 2199–2211.

Knittle, E., and Williams, Q. (1993) High-pressure raman-spectroscopy of $ZrSiO_4$: Observation of the zircon to scheelite transition at 300 K. American Mineralogist, 78, 245–252.

Koeman, E.C., Simonetti, A., Chen, W., and Burns, P.C. (2013) Oxygen isotope composition of Trinitite postdetonation materials. Analytical Chemistry, 85(24), 11913–11919.

Kowitz, A., Gueldemeister, N., Reimold, W.U., Schmitt, R.T., and Wuennemann, K. (2013a) Diaplectic quartz glass and $SiO_2$ melt experimentally generated at only 5 GPa shock pressure in porous sandstone: Laboratory observations and mesoscale numerical modeling. Earth and Planetary Science Letters, 384, 17–26.

Kowitz, A., Schmitt, R.T., Reimold, W.U., and Hornemann, U. (2013b) The first MEMIN shock recovery experiments at low shock pressure (5-12.5 GPa) with dry, porous sandstone. Meteoritics & Planetary Science, 48(1), 99–114.

Kumar, P., Saxena, N., Singh, F., and Agarwal, A. (2012) Nanotwinning in CdS quantum dots. Physica B: Condensed Matter, 407(17), 3347–3351.

Kusaba, K., Syono, Y., Kikuchi, M., and Fukuoka, K. (1985) Shock behavior of zircon—phase-transition to scheelite structure and decomposition. Earth and Planetary Science Letters, 72(4), 433–439.

Lambert, P. (1979) Fractures induced by shock in quartz and feldspar. Mineralogical Magazine, 43(328), 527–533.

Langenhorst, F. (1994) Shock experiments on pre-heated alpha-quartz and beta-quartz. 2. X-ray and TEM investigations, Earth and Planetary Science Letters, 128(3-4), 683–698.

Langenhorst, F., and Deutsch, A. (1994) Shock experiments on pre-heated alpha-quartz and beta-quartz. 1. Optical and density data. Earth and Planetary Science Letters, 125(1-4), 407–420.

Lee, W.E., and Rainforth, W.M. (1994) Ceramic Microstructures: Property Control byProcessing, 590 p. Chapman & Hall, London.

Lenz, C., Nasdala, L., Talla, D., Hauzenberger, C., Seitz, R., and Kolitsch, U. (2015) Laser-induced REE$^{3+}$ photoluminescence of selected accessory minerals—An "advantageous artefact" in Raman spectroscopy. Chemical Geology, 415, 1–16.

Leroux, H., Reimold, W.U., Koeberl, C., Hornemann, U., and Doukhan, J.C. (1999) Experimental shock deformation in zircon: a transmission electron microscopic study. Earth and Planetary Science Letters, 169(3-4), 291–301.

McMillan, P.F., Wolf, G.H., and Lambert, P. (1992) A raman-spectroscopic study of shocked single crystalline quartz. Physics and Chemistry of Minerals, 19(2), 71–79.

Muddle, B.C., and Hannink, R.H.J. (1986) Crystallography of the tetragonal to monoclinic transformation in MgO-partially-stabilized zirconia. Journal of the American Ceramic Society, 69(7), 547–555.

Nakano, Y., Goto, K., Matsui, T., Tada, R., and Tajika, E. (2008) PDF orientations in shocked quartz grains around the Chicxulub crater. Meteoritics & Planetary Science, 43, 745–760.

Ostertag, R. (1983) Shock experiments on feldspar crystals. Journal of Geophysical Research, 88, B364–B376.

Parekh, P.P., Semkow, T.M., Torres, M.A., Haines, D.K., Cooper, J.M., Rosenberg, P.M., and Kitto, M.E. (2006) Radioactivity in Trinitite six decades later. Journal of Environmental Radioactivity, 85, 103–120.

Pavlik, R.S., Holland, H.J., and Payzant, E.A. (2001) Thermal decomposition of zircon refractories. Journal of the American Ceramic Society, 84, 2930–2936.

Piazolo, S., Austrheim, H., and Whitehouse, M. (2012) Brittle-ductile microfabrics in naturally deformed zircon: Deformation mechanisms and consequences for U-Pb dating. American Mineralogist, 97, 1544–1563.

Pidgeon, R.T., Nemchin, A.A., and Kamo, S.L. (2011) Comparison of structures in zircons from lunar and terrestrial impactites. Canadian Journal of Earth Sciences, 48, 107–116.

Ravindran, T.R., and Yadav, K. (2015) Re-examination of high pressure orthorhombic-I phase of ZrO$_2$ by Raman spectroscopy. The European Physical Journal B, 88, 1434–6036.

Reimold, W.U., Leroux, H., and Gibson, R.L. (2002) Shocked and thermally metamorphosed zircon from the Vredefort impact structure, South Africa: a transmission electron microscopic study. European Journal of Mineralogy, 14, 859–868.

Rhodes, R. (1986) The Making of the Atomic Bomb. Simon and Schuster, New York.

Ross, C.S. (1948) Optical properties of glass from Alamogordo, New Mexico. American Mineralogist, 33, 360–362.

Schmieder, M., Reimold, W.U., Buchner, E., Khirfan, M., Salameh, E., and Khoury, H. (2011) Shock-metamorphic microfeatures in chert from the Jebel Waqf as Suwwan impact structure, Jordan. Meteoritics & Planetary Science, 46(4), 574–586.

Staritzky, E. (1950) Thermal effects of atomic bomb explosions on soils at Trinity and Eniwetok. Department of General Chemistry. Los Alamos Scientific Laboratory. New Mexico, Report No. LA-1126.

Stoffler, D. (1971) Progressive metamorphism and classification of shocked and brecciated crystalline rocks at impact craters. Journal of Geophysical Research, 76, 5541–5551.

Stoffler, D., and Langenhorst, F. (1994) Shock metamorphism of quartz in nature and experiment. 1. Basic observation and theory. Meteoritics, 29(2), 155–181.

Timms, N.E., Erickson, T.M., Schmieder, M., Tohver, E., and Pearce, M. (2014) Shock recrystallisation and decomposition of zircon. Meteoritics & Planetary Science, 49, A397–A397.

Trepmann, C.A. (2008) Shock effects in quartz: Compression versus shear deformation—An example from the Rochechouart impact structure, France. Earth and Planetary Science Letters, 267, 322–332.

Trepmann, C.A., and Spray, J.G. (2006) Shock-induced crystal-plastic deformation and post-shock annealing of quartz: microstructural evidence from crystalline target rocks of the Charlevoix impact structure, Canada. European Journal of Mineralogy, 18(2), 161–173.

Turner, D., Langenhorst, F., and Pollok, K. (2014) Martensitic mechanism of the zircon-to-reidite transformation. Meteoritics & Planetary Science, 49, A406–A406.

Wallace, C., Bellucci, J.J., Simonetti, A., Hainley, T., Koeman, E.C., and Burns, P.C. (2013) A multi-method approach for determination of radionuclide distribution in Trinitite. Journal of Radioanalytical and Nuclear Chemistry, 298(2), 993–1003.

Wittmann, A., Kenkmann, T., Schmitt, R.T., and Stoffler, D. (2006) Shock-metamorphosed zircon in terrestrial impact craters. Meteoritics & Planetary Science, 41(3), 433–454.

Zanetti, M., Wittmann, A., Nemchin, A., Carpenter, P., Vicenzi, E.P., and Jolliff, B. (2014) Decomposition of zircon in mistastin lake impact melt glass: an integrated sims, hyperspectral-cl, raman and EPMA study. Meteoritics & Planetary Science, 49, A449–A449.